aerospace

MDPI

Article

Numerical Investigation on Cooling Performance of Rectangular Channels Filled with X-Shaped Truss Array Structures

Lei Xi, Jianmin Gao, Liang Xu *, Zhen Zhao, Zhengheng Yang and Yunlong Li

State Key Laboratory for Manufacturing Systems Engineering, Xi'an Jiaotong University, Xi'an 710049, China; xilei100@mail.xjtu.edu.cn (L.X.); gjm@mail.xjtu.edu.cn (J.G.); zhaozhen.900803@stu.xjtu.edu.cn (Z.Z.); zhengheng.yang@stu.xjtu.edu.cn (Z.Y.); ylongli@mail.xjtu.edu.cn (Y.L.)
* Correspondence: xuliang@mail.xjtu.edu.cn; Tel.: +86-18691861949

Abstract: In this study, different layout schemes for an X-shaped truss array channel are designed to explore the application of an X-shaped truss array structure in the mid-chord region of turbine blades. The flow and heat transfer performance of X-shaped truss array channels for three layout schemes are numerically investigated. The influence laws of the subchannel height ratio (*h/H*, 0.2 to 0.4) regarding the cooling performance of the channel with three subchannels are also analyzed. Then, the corresponding heat transfer and friction correlations are obtained. The results show that the layout scheme has significant effects on the flow performance, heat transfer performance and comprehensive thermal performance of X-shaped truss array channels. Among the three layout schemes of X-shaped truss array channels, the single channel has the best flow performance, while the channel with three subchannels has the best heat transfer performance and a comprehensive thermal performance. At different Reynolds numbers, the average Nusselt numbers and comprehensive thermal coefficients of the X-shaped truss array channel with three subchannels range from 38.94% to 63.49% and 27.74% to 46.49% higher than those of a single channel, respectively, and from 5.68% to 18.65% and 11.61% to 21.96% higher than those of the channel with two subchannels, respectively. For the channel with three subchannels, the subchannel height ratio has a great influence on the flow performance, but has a relatively small influence on the heat transfer performance and comprehensive thermal performance of the channel. With the increase in subchannel height ratio, the friction coefficient and average Nusselt number of the channel with three subchannels both show a trend of first increasing and then decreasing, while the comprehensive thermal coefficient shows a slow decreasing trend at higher Reynolds numbers. As a result of comprehensive consideration, the channel with three subchannels at a subchannel height ratio of 0.25 has a better overall cooling performance and is more suitable for cooling the mid-chord region of gas turbine blades. The results may provide a reference for the application of truss array structures in the internal cooling of advanced high-temperature turbine blades in the future.

Keywords: turbine blade; cooling channel; X-shaped truss array; flow and heat transfer; empirical correlations

check for updates

Citation: Xi, L.; Gao, J.; Xu, L.; Zhao, Z.; Yang, Z.; Li, Y. Numerical Investigation on Cooling Performance of Rectangular Channels Filled with X-Shaped Truss Array Structures. *Aerospace* **2022**, *9*, 405. https://doi.org/10.3390/aerospace9080405

Academic Editor: Qiang Zhang

Received: 17 May 2022
Accepted: 25 July 2022
Published: 27 July 2022

Publisher's Note: MDPI stays neutral with regard to jurisdictional claims in published maps and institutional affiliations.

Copyright: © 2022 by the authors. Licensee MDPI, Basel, Switzerland. This article is an open access article distributed under the terms and conditions of the Creative Commons Attribution (CC BY) license (https://creativecommons.org/licenses/by/4.0/).

1. Introduction

Advanced gas turbine blades operate in harsh environments up to temperatures of 2000 K and need to be cooled efficiently [1]. In pursuit of efficient cooling, various cooling structures are arranged inside and outside the high-temperature blades of advanced gas turbines [2]. Traditional turbine blade cooling structures include film cooling and impingement cooling at the leading edge region, rib-turbulated cooling at the mid-chord region, and pin-fin cooling and slot cooling at the trailing edge region [3]. Although these traditional cooling structures have shown relatively good cooling effects in modeling studies, they cannot effectively improve the structural strength of turbine blades. Specifically, film cooling and slot cooling may directly weaken the structural strength of turbine blades [4,5]. Impingement cooling has the problem of uneven heat transfer distribution, which may cause excessive thermal stress and affect the structural strength of turbine blades [6]. Rib-turbulated cooling can improve the ability to resist the tensile stress and compressive stress of turbine blades, but still cannot meet the strength requirements of advanced high-temperature turbine blades [7]. Pin-fin cooling has the problem of large flow resistance and a relatively lower cooling effect when applied to the narrow trailing edge region, and the caused higher temperature may also reduce the structural strength of the turbine blades [8]. In sum, the cooling design of turbine blades is faced with the challenge of combining a high cooling efficiency with high structural strength. Therefore, new cooling structures with high-efficiency cooling technology and high structural strength are urgently needed to ensure the safe and reliable operation of gas turbine blades [9].

Truss structures are multi-functional topology optimization structures that emerged with the rapid development of 3D printing technology in recent years [10] and have gradually been applied to various disciplines and industries [11,12]. The most widely used truss structures are the Kagome-shaped truss structure, pyramid-shaped truss structure and tetrahedron-shaped truss structure [13]. The literature has proved that truss structures have excellent mechanical properties, such as high toughness, high specific stiffness, high specific strength, noise and vibration reductions, and high energy absorption [14–16]. In addition, many studies have reported that truss structures have an excellent convective heat transfer capacity and thermal conductivity performance [17,18]. If the truss structures are filled into the cooling channels of gas turbine blades, it is expected that the structural strength and heat transfer effect of the blades would be intensified.

Since 2003, a number of studies have been performed on the thermal performance and cooling performance of various truss array structures [19,20]. Many investigators used non-metallic resin materials to study the heat transfer enhancement caused only by the fluid disturbance effect of truss structures. Kim et al. [21] studied the flow separation and vortex distribution caused by polycarbonate tetrahedral truss structures, and stated that horseshoe vortexes and arch-shaped vortexes are formed around the truss rods. Wei et al. [22] experimentally measured the equivalent thermal conductivity of a C/SiC tetrahedral truss array structure under various boundary conditions. Gao et al. [23,24] reported that the comprehensive heat transfer capacity of composite truss structures is significantly better than that of other heat dissipation media. Dixit et al. [25] investigated the forced-convection and heat transfer characteristics of various resin truss structures under the conditions of a low Reynolds number and constant temperature using a numerical approach and summarized that the heat transfer capacity of a body-centered cubic truss is better than that of open-cell foam heat sinks. Xu et al. [26] numerically researched the heat transfer and flow behavior of a rectangular channel filled with a staggered resin Kagome array, and reported that the rise in the Reynolds number and truss rod diameter both showed a significant heat transfer enhancement effect. Many researchers have comprehensively considered the effects of fluid disturbance and heat conduction on the heat transfer enhancement of truss structures. Qian et al. [27] studied the boiling heat transfer performance of a microchannel heat exchanger with different nonuniform truss structures and stated that the heat transfer effect of nonuniform truss structures is inferior to that of uniform truss structures. Son et al. [28] introduced tetrahedral truss structures into the thermal management of a lithium-ion battery and pointed out that tetrahedral truss structures can provide a good cooling solution for the heat dissipation of lithium batteries. You et al. [29] stated that truss structures have high cooling abilities and can be used as a thermal metamaterial, according to the cooling experiment results. Yun et al. [30] analyzed the thermo-fluid performance of graded truss array channels. Their results show that the channels with W-type and V-type graded truss structures exhibit the best and worst thermo-fluid performance, respectively. Kaur et al. [31,32] compared the thermal-hydraulic performance of metal foams and metal truss structures using an experimental method and pointed out that the heat transfer coefficient values of truss structures are higher than those of stochastic metal foams. Zhou et al. [33] obtained a kind of truss cooling channel with an excellent heat transfer and bearing performance using the topology optimization multi-scale and multi material methods. Lai et al. [34] analyzed the heat transfer behaviors of a heat exchanger filled with various truss array structures. Their results show that the direction of truss structures has great impact on the flow and heat transfer performance of the heat exchanger, and the star-type truss structure can best meet the performance requirements of the heat exchanger.

Recently, several studies have been published on the cooling performance of gas turbine blade internal cooling channels filled with various truss array structures [35]. Xu et al. [36,37] compared the heat transfer effect of different truss array structures under the scale of gas turbine blades, and recommended that X-shaped truss structures have the best heat transfer performance. Kaur et al. [38] studied the flow and heat transfer performance of a gas turbine blade trailing edge filled with four different truss array structures, and pointed out that the truss array structure of the face diagonal-cube has the highest pressure drop as well as the highest heat transfer coefficient at the same Reynolds number. Liang et al. [39] researched the flow and heat transfer performance of body centered cubic, Kagome and X-type truss structures in the cooling channel of a gas turbine trailing edge, and stated that the induced vortex size significantly affects the degree of heat transfer enhancement in the cooling channel.

According to the above literature review, although much attention has been directed toward the thermal performance and cooling performance of different kinds of truss structures, fewer investigations have been conducted regarding the cooling performance of truss structures under the scale and conditions of gas turbine blades. The problem of how to apply a high-performance truss array structure to the mid-chord region of gas turbine blades has not been well resolved. Consequently, it is necessary to study the cooling performance of different layout schemes of the gas turbine blade mid-chord region filled with high-performance truss array structures.

In this investigation, different layout schemes of an X-shaped truss array channel were designed on the basis of the optimization results in [40,41] to explore the application of an X-shaped truss array structure in the mid-chord region of turbine blades. Firstly, the flow and heat transfer performance of X-shaped truss array channels for three layout schemes were numerically investigated. Secondly, the influence laws of subchannel height ratio (h/H, 0.2 to 0.4) on the cooling performance of the channel of Scheme 3 were analyzed in detail. Finally, the heat transfer and friction correlations of X-shaped truss array channels under different layout schemes were separately fitted. The results may provide a reference for the application of truss array structures in the internal cooling of advanced high-temperature turbine blades in the future.

2. Research Object

2.1. Physical Model

The cooling channel in this investigation was modeled from a F-class gas turbine blade mid-chord region [42]. The aspect ratio of the mid-chord region was about two. For convenience, the cooling channel of the mid-chord region was simplified to a rectangular channel with an aspect ratio of two. The length (L), width (W), height (H) and wall thickness (δ) of the channel were 120 mm, 40 mm, 20 mm and 1 mm, respectively. The cooling channel was further divided into three subchannels to provide different layout schemes. The height of the subchannel is denoted by h. As displayed in Figure 1a, the X-shaped truss units were arranged in the cooling channels in an array. The structural parameters of the X-shaped truss array include the diameter ratio (d/h) and inclination angle (β) of the truss rods, the characteristic length ($C = h/\tan(\beta)\times\sin(45^\circ)$), transverse spacing ratio (X_s/C) and streamwise spacing ratio (Z_s/C) of the truss elements. In this investigation, $\beta = 45^\circ$, $d/h = 0.248$, $X_s/C = 2.482$ and $Z_s/C = 1.946$, which is the optimization result at a high Reynolds number ($Re = 60{,}000$) in Reference [41]. The specific structural parameters for different layout schemes were calculated from the above optimization result. As shown in

Figure 1b–d, three layout schemes were designed for the X-shaped truss array structure arranged in the internal cooling channel of the gas turbine blade mid-chord region. For Scheme 1 (single channel), the X-shaped truss array was directly arranged in the cooling channel. As the characteristic size of the truss unit is positively related to its height, the length and width of the truss unit in Scheme 1 were relatively large, and only one row and four columns of truss units were arranged in the cooling channel of Scheme 1. For Scheme 2 (two subchannels), a 1 mm-thick divider plate was added to the mid-section of the original channel to divide it into two subchannels, and the subchannel height ratio (*h/H*) was 0.475. The X-shaped truss array structure was arranged in each subchannel. According to the subchannel height ratio and the optimal spacing of the X-shaped truss array mentioned above, two rows and eight columns of truss units were arranged in the cooling channel of Scheme 2. For Scheme 3 (three subchannels), two 1 mm-thick divider plates were added to the original channel to divide it into three subchannels. The X-shaped truss array structure was only arranged in the two subchannels close to the wall. The subchannel height ratio of the two subchannels near the wall for Scheme 3 ranged from 0.2 to 0.4. According to the optimization result mentioned above, from two to five rows and nine to eighteen columns of truss units were arranged in each of the two subchannels near the wall for the different *h/H* of Scheme 3, respectively. The detailed structural parameters of the X-shaped truss array channels for different layout schemes are listed in Table 1.

2.2. Data Reduction

The equivalent diameter D of the channel is:

$$D = 2WH/(W + H) \tag{1}$$

where W is the channel width; H is the channel height.

The Reynolds number Re is expressed as:

$$Re = uD/v \tag{2}$$

where u and v are the inlet velocity and kinematic viscosity of cooling air.

The wall Nusselt number Nu is calculated by:

$$Nu = qD/[(T_{\mathrm{w}} - T_{\mathrm{f}})\lambda] \tag{3}$$

where q and T_{w} are the wall heat flux and wall temperature; T_{f} is the local bulk fluid temperature; λ is the thermal conductivity of cooling air.

The friction coefficient f is written as:

$$f = \Delta pD/(2\rho Lu^2) \tag{4}$$

where ρ is the density of cooling air; Δp is the pressure difference across the channel; L is the channel length.

The comprehensive thermal coefficient F is computed by:

$$F = (Nu_{\mathrm{ave}}/Nu_0)/(f/f_0)^{1/3} \tag{5}$$

where Nu_{ave} is the average Nusselt number of the X-shaped truss array channel; $Nu_0 = 0.023Re^{0.8}Pr^{0.4}$ and $f_0 = (1.58\ \ln Re - 3.28)^{-2}$ are the average Nusselt number and friction coefficient of the smooth channel.

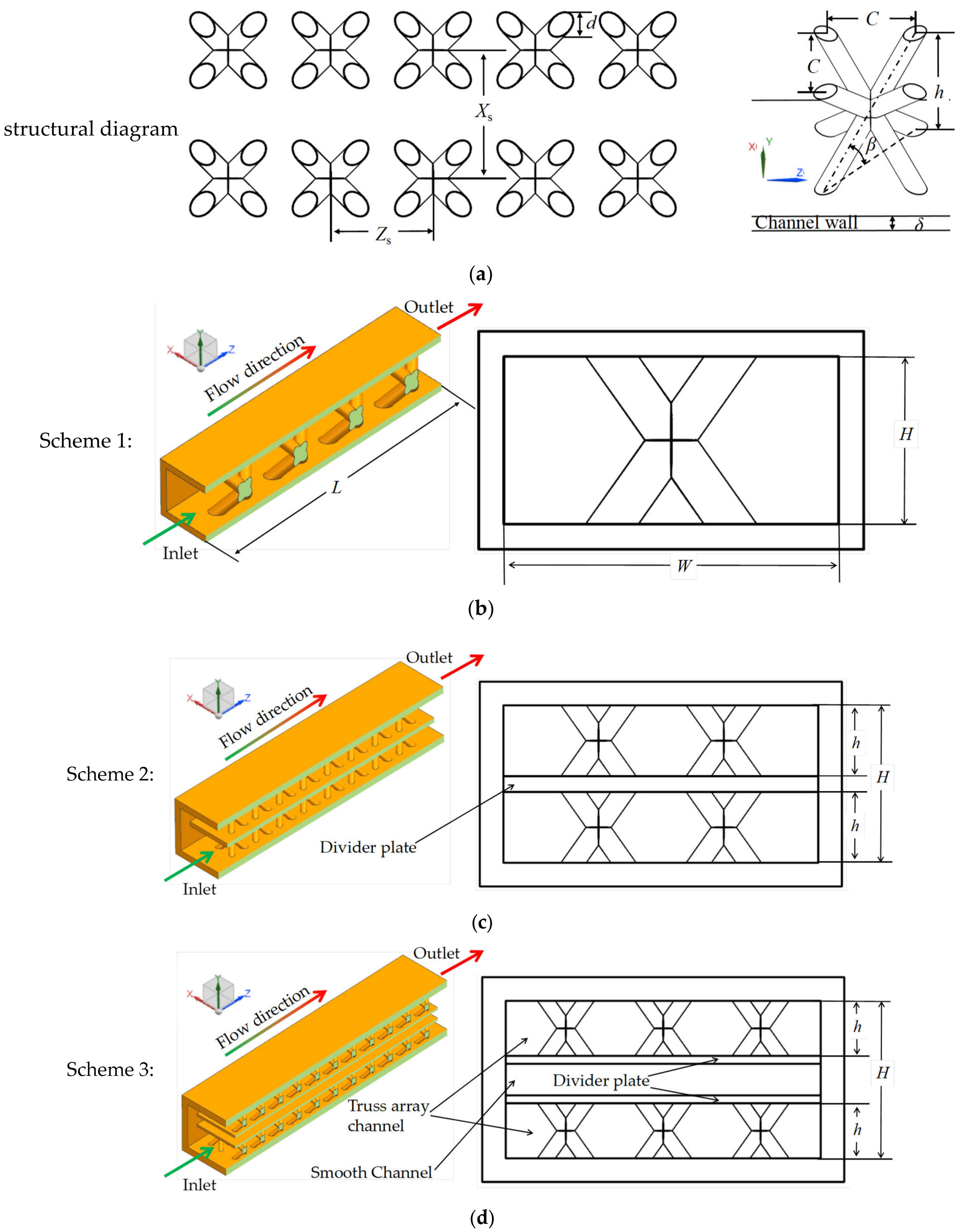

Figure 1. Research object: (**a**) structural diagram; (**b**) Scheme 1: single channel; (**c**) Scheme 2: two subchannels; (**d**) Scheme 3: three subchannels.

Table 1. Structural parameters of X-shaped truss array channels for different layout schemes (based on the optimization results at Re = 60,000 in [41]).

Channel Types	h/H	Row Number	Column Number
Scheme 1: single channel	1	1	4
Scheme 2: two subchannels	0.475	2	8
Scheme 3: three subchannels	0.20	5	18
Scheme 3: three subchannels	0.25	4	15
Scheme 3: three subchannels	0.30	3	12
Scheme 3: three subchannels	0.35	3	11
Scheme 3: three subchannels	0.40	2	9

3. Numerical Methods

3.1. Numerical Model

Figure 2 demonstrates the numerical calculation model of the X-shaped truss array channel (Scheme 3: h/H = 0.35) used in this investigation. As shown in Figure 2a, the numerical model includes the solid and fluid domains of the X-shaped truss array channel and the fluid domains of the smooth channel extended from the inlet and outlet with a length of 200 mm. Since the X-shaped truss array channel is symmetrically distributed about the mid-section, for the convenience of numerical calculation, the numerical model in this study was half of the X-shaped truss array channel. The grid models of the X-shaped truss array channel were divided by an unstructured grid. The grid division was completed in the Meshing module of Workbench. The unstructured grid models for the solid domain and fluid domain of the X-shaped truss array channel are shown in Figure 2b. The solid domain is composed of pure tetrahedral meshes. The fluid domain is composed of tetrahedral meshes for the main body and prismatic meshes for the boundary layer near channel walls. The layer number and height ratio of the prismatic meshes were 15 and 1.2. The initial height of prismatic meshes was 0.001 mm, and the corresponding y^+ was less than 1. The minimum size of tetrahedral meshes for the refined regions of truss rods and their adjacent regions was about 0.03 mm. The maximum size of tetrahedral meshes was adjusted to control the total mesh number. Finally, the mesh nodes on the fluid–solid interface were matched and all meshes were smoothed to improve the grid quality and the numerical calculation precision. In this study, five sets of grid models were divided to execute the verification of grid independence. The maximum size of tetrahedral meshes varied from 0.8 mm to 2.4 mm, and the corresponding total mesh number ranged from 8.32 million to 4.01 million. According to the verification results in Table 2, the total mesh number of 6.86 million with a maximum mesh size of 1.2 mm is most suitable for the numerical calculations of the X-shaped truss array channel in this study.

Table 2. Verification of grid independence (Scheme 3: h/H = 0.35, Re = 30,000).

Maximum Mesh Size/mm	Total Mesh Number/Million	Nu_{ave}	Difference/%
2.4	4.01	163.78	-
2.0	4.63	181.64	10.90
1.6	5.39	196.14	7.98
1.2	6.86	207.22	5.65
0.8	8.32	210.13	1.40

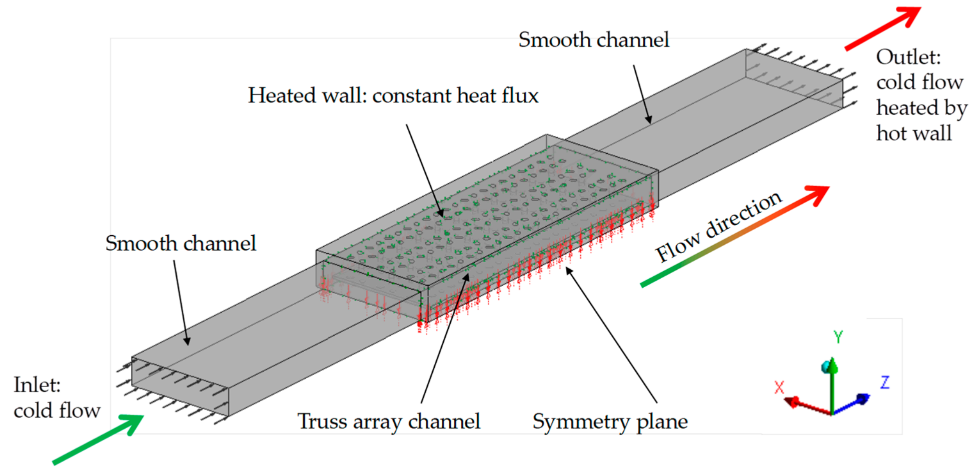

(**a**)

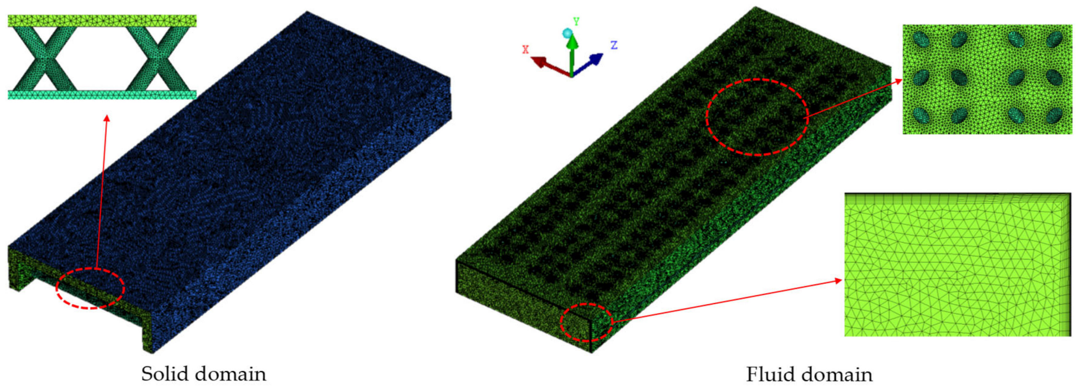

(**b**)

Figure 2. Numerical calculation model (Scheme 3: *h*/*H* = 0.35): (**a**) numerical model; (**b**) grid model.

3.2. Numerical Calculation Method

The coupled heat transfer numerical approach was used to analyze the flow and heat transfer performance of X-shaped truss array channels in this investigation. The numerical calculations were completed with CFX software (V19.5, ANSYS Inc., Pittsburgh, PA, USA). In the numerical calculations, the fluid flow in the X-shaped truss array channel was assumed to be steady, incompressible, 3D turbulent flow, without considering the effect of gravity. The corresponding governing equations [41] are as follows:

$$\frac{\partial V_j}{\partial x_j} = 0 \tag{6}$$

$$\frac{\partial(\rho V_i V_j)}{\partial x_j} = -\frac{\partial p}{\partial x_i} + \frac{\partial}{\partial x_j}\left[(\mu + \mu_t)\left(\frac{\partial V_i}{\partial x_j} + \frac{\partial V_j}{\partial x_i}\right)\right] \tag{7}$$

$$\frac{\partial(\rho T V_j)}{\partial x_j} = \frac{\partial}{\partial x_j}\left[\left(\frac{\lambda}{c_p} + \frac{\mu_t}{Pr_t}\right)\frac{\partial T}{\partial x_j}\right] \tag{8}$$

where Pr_t is the turbulent Prandtl number and μ_t is the turbulent viscosity.

The fully implicit coupled multigrid was used to solve the Reynolds-averaged Navier Stokes equations. The bounded central difference scheme of the finite difference method was utilized to discretize the governing equations [41]. In CFX-Pre, the Total Energy equation with the option of Incl. Viscous Work Term was selected for the heat transfer scheme, and the high-resolution scheme was chosen for the turbulence numerics scheme and advection scheme. Three turbulence models of k-ω, k-ε and SST k-ω were tested to calculate the turbulent flow in the channel. The enhanced wall treatment method was adopted for the near-wall treatment of the k-ε model. The near-wall model method was adopted to solve the near-wall turbulent flow for the low-Reynolds-number turbulence models such as k-ω and SST k-ω. Based on the authors' previous findings [40,41], the SST k-ω turbulence model combined with the near-wall model method was preferentially chosen to calculate the turbulent flow in the X-shaped truss array channels. For the solid domain of the X-shaped truss array channel, only the heat conduction equation was solved. When the Root Mean Square residuals of governing equations were lower than 10^{-6} or the user-built monitoring point (channel wall average temperature) did not change, the numerical calculations reached the convergence condition and were terminated.

3.3. Boundary Conditions

The numerical simulations in this investigation are steady-state solution processes, and the boundary conditions were set as follows: As shown in Figure 2a, the mid-section of the channel was set as a symmetrical boundary condition. The cooling air, with a static temperature of 298.15 K, a turbulence level of 5% and a uniform velocity, first enters the smooth channel upstream along the normal direction of the channel inlet, then flows through the X-shaped truss array channel to cool it, and finally flows out of the smooth channel downstream. The fluid–fluid interfaces were created between the fluid domain of the X-shaped truss array channel and the two smooth channels upstream and downstream to form a complete flow process. The inlet velocity was computed by the inlet Reynolds number (*Re*, 10,000 to 60,000). The channel outlet was set as a static pressure outlet. The channel outlet pressure was the averaged value over the whole outlet area, with a fluctuation range of 5% at different positions. The relative value of average static pressure of the channel outlet was set to 0 kPa in CFX-Pre, since the reference pressure was set to 101 kPa. The outer walls of the solid domain were heated by a constant heat flux of 3000 $W \cdot m^{-2}$. The relevant surfaces of fluid domain and solid domain were set as fluid–solid interfaces. The same heat flux and temperature were transferred from the inner wall of the solid domain to the wall of fluid domain by the fluid-solid interfaces. Finally, the cooling air takes away the heat from the channel wall and was discharged from the channel outlet. To speed up the convergence process, initialization settings were created for the fluid domain and solid domain, respectively. The initial temperature of 298.15 K, initial static pressure of 101 kPa, initial turbulence level of 5%, and initial normal velocity based on the inlet Reynolds number were set for the entire fluid domain. Under these initial conditions, the density, dynamic viscosity, thermal conductivity, specific heat capacity at constant pressure and Prandtl number of cooling air at the channel inlet were 1.172 $kg \cdot m^{-3}$, 0.0000184 $Pa \cdot s$, 0.0262 $W \cdot m^{-1} \cdot K^{-1}$, 1.007 $kJ \cdot kg^{-1} \cdot K^{-1}$, and 0.705, respectively. The initial temperature of the entire solid domain was set to 298.15 K. Additionally, in order to avoid the divergence of numerical calculation, the auto timescale option was selected for the timescale control, the conservative option was selected for the length scale of the time step, and the relevant timescale factor was set to 1.

3.4. Verification of Numerical Method

The experimental data of the X-shaped truss array channel with d/H = 0.2, X_s/C = 2 and Z_s/C = 2 in [41] were used to verify the numerical method in this investigation. A comparison of the results for the numerical calculated average Nusselt number by different turbulence models and the experimental values in [41] is displayed in Figure 3. It can be seen that the variation trends of the average Nusselt number with the Reynolds number calculated by the three turbulence models (SST k-ω, standard k-ε and standard k-ω) are very close to the variation trends of the average Nusselt number with the Reynolds number measured by the experiment. The calculated values of standard k-ε are higher than the experimental values, and the calculated values of SST k-ω and standard k-ω are lower than the experimental values. It is worth noting that the calculated values of SST k-ω are closest to the experimental values (maximum deviation is 12.7%), which is because SST k-ω has the advantages of a standard k-ε and standard k-ω. The above results indicate that the numerical method with an SST k-ω turbulence model in this investigation can accurately analyze the heat transfer performance of X-shaped truss array channels.

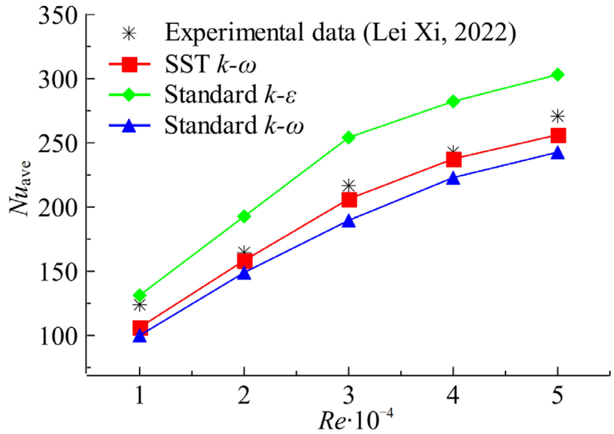

Figure 3. Verification of numerical methods based on the experimental data in [41].

4. Results and Discussion

4.1. Flow Performance

Figure 4 demonstrates the flow field distributions in X-shaped truss array channels of different layout schemes (see Table 1) at Re = 30,000. To clearly show the results, only the flow fields in half of the channels are shown in the figure due to the symmetrical distribution of the channels at the mid-section. The flow field was visualized by the λ_2 criterion method, which is one of the most accurate vortex core display technologies in CFX-Post [43]. As displayed in Figure 4, the vortex cores in the X-shaped truss array channels of the three layout schemes are mainly distributed around the truss rods. This is due to the fluid disturbing effect of the truss rod, meaning that a horseshoe vortex is formed around each truss rod. For Scheme 1, the velocity of the vortex cores around the first two columns of truss units is higher due to the entrance effect [40], while the velocity of the vortex cores around the latter two columns of truss units is lower. For Scheme 2 and Scheme 3, the velocity of the vortex cores around the first column of truss units is much higher; then, the velocity of the vortex cores gradually decreases from the second column to the fourth column of truss units. After the fourth column of truss units, the velocity of the vortex cores basically no longer changes, which indicates that from here the flow in the X-shaped truss array channel enters a fully developed stage. Overall, the size and velocity of the vortex cores formed around the truss rods in the channel of Scheme 1 are the largest, followed by those formed in the channel of Scheme 2, and the size and velocity of the vortex cores formed in the channel of Scheme 3 are the smallest. However, from Scheme 1 to Scheme 3, the number of truss units in the channel greatly increased. Therefore, it is difficult to intuitively judge which layout scheme of X-shaped truss array channel has the best flow performance, and this subject requires further quantitative analysis.

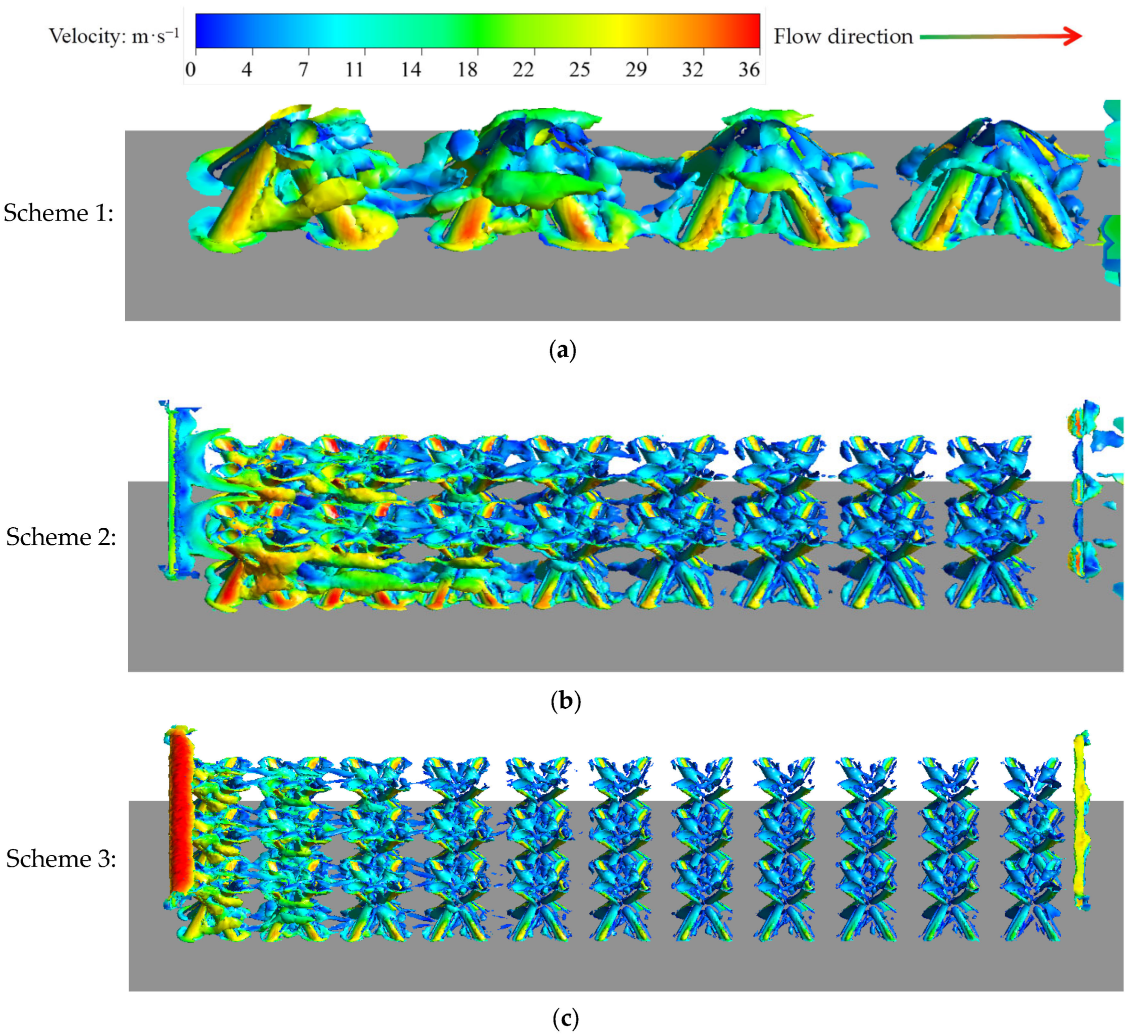

Figure 4. Flow field distributions in X-shaped truss array channels at different layout schemes (*Re* = 30,000): (**a**) Scheme 1; (**b**) Scheme 2; (**c**) Scheme 3.

Figure 5 illustrates the change curves of friction coefficients with an inlet Reynolds number for the three layout schemes of X-shaped truss array channels, where Scheme 3 refers specifically to the channel h/H = 0.35. As shown in Figure 5, the friction coefficients of the three layout schemes of X-shaped truss array channels first slightly decrease and then remain basically unchanged with the increase in Reynolds number. This is because the friction coefficient is directly proportional to the pressure drop and inversely proportional to the square of the inlet air velocity, as defined in Equation (4). Meanwhile the inlet air velocity is positively correlated with the Reynolds number. For a cooling channel, when the Reynolds number increases, the pressure drops and the inlet air velocity increases correspondingly. Therefore, the friction coefficient is the result of the balance between the increase rate of the pressure drop and the increase rate of the Reynolds number. For the X-shaped truss array channels in this study, the change rate of the square of inlet air velocity with a Reynolds number is greater than that of the pressure drop with a Reynolds number; thus, the friction coefficients show decreasing trends with the increase in Reynolds number. Figure 5 also shows that the friction coefficient of the X-shaped truss array channel of Scheme 2 is the largest; that is, the flow performance of the channel of Scheme 2 is the worst. The friction coefficient of the X-shaped truss array channel of Scheme 1 is the smallest; thus, the flow performance of the channel of Scheme 1 is the best. As shown in the quantitative analysis results, when the Reynolds number changes from 10,000 to 60,000, the friction coefficients of the X-shaped truss array channels of Scheme 1, Scheme 2 and Scheme

3 decrease by 3.22%, 2.99% and 10.45%, respectively. At different Reynolds numbers, the friction coefficient of the X-shaped truss array channel of Scheme 1 is 32.32% to 33.96% and 21.91% to 28.09% lower than those in the channels of Scheme 2 and Scheme 3, respectively. In summary, the layout scheme has a relatively high influence on the flow performance of the X-shaped truss array channel, while the influence of Reynolds number on the flow performance of the X-shaped truss array channel is not significant. From the perspective of friction coefficient reduction, the layout scheme of the X-shaped truss array channel of Scheme 1 is the best.

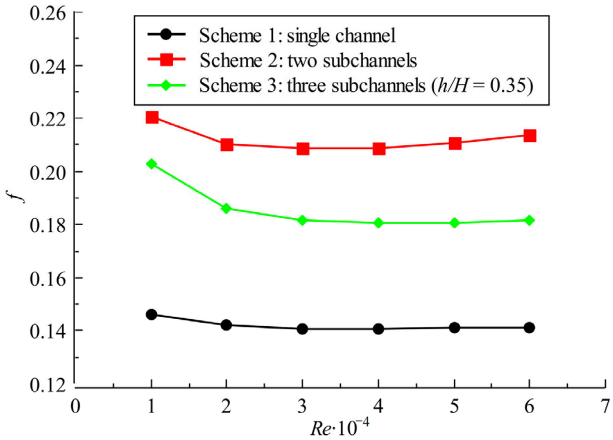

Figure 5. Comparison of flow performance of X-shaped truss array channels at different layout schemes.

Figure 6 illustrates the flow field distributions in X-shaped truss array channels of Scheme 3 at different subchannel height ratios (Re = 30,000). It can be seen in Figure 6 that, as the subchannel height ratio increases, the size of the truss unit also increases, which enhances the flow-disturbing effect of each truss unit, resulting in an increase in the size and velocity of the vortex cores formed around each truss unit in the channels. Similarly, since the increase in subchannel height ratio also reduces the number of truss units in the channel, it is difficult to intuitively judge the influence law of the subchannel height ratio on the flow performance of the X-shaped truss array channels. At the same time, it can be found that with the increase in subchannel height ratio, the position where the fluid flow in the channel enters the fully developed stage is farther from the channel inlet. In addition, for the channels of Scheme 3 at different subchannel height ratios, a larger-sized transverse vortex core is formed at the inlet of each channel, and a smaller-sized transverse vortex core is formed at the outlet of each channel. Meanwhile, with the increase in subchannel height ratio, the size of the transverse vortex core at the inlet of the channel gradually decreases, while the size of the transverse vortex core at the outlet of the channel almost remains unchanged; the velocity of the transverse vortex cores at the channel inlet and outlet first increases and then decreases, and reaches its maximum at h/H = 0.35.

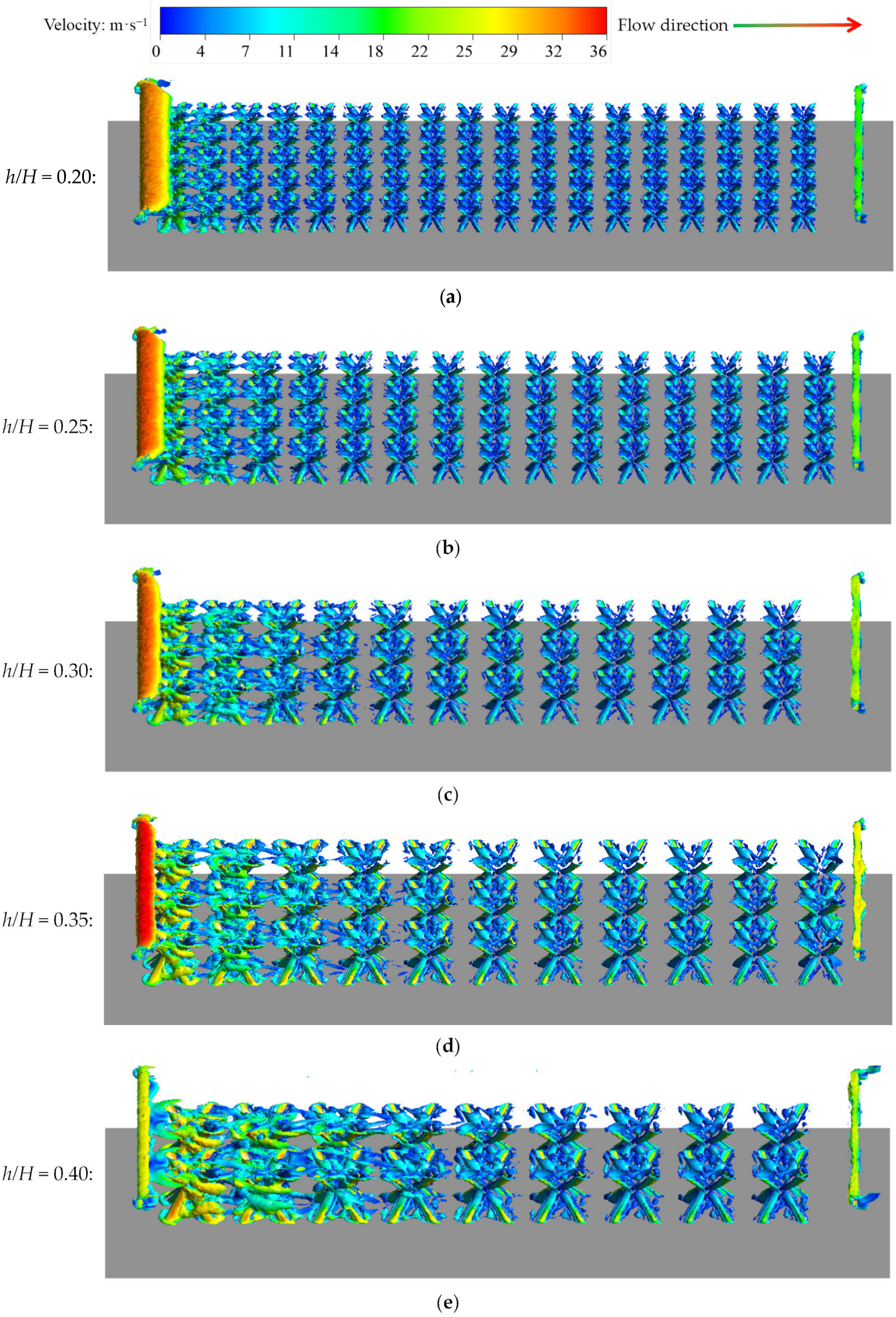

Figure 6. Flow field distributions in X-shaped truss array channels of Scheme 3 at different h/H (Re = 30,000): (**a**) h/H = 0.20; (**b**) h/H = 0.25; (**c**) h/H = 0.30; (**d**) h/H = 0.35; (**e**) h/H = 0.40.

Figure 7 demonstrates the influence law of subchannel height ratio on the friction coefficients of X-shaped truss array channels of Scheme 3 at different Reynolds numbers. It can be seen from Figure 7 that, under different Reynolds numbers, the friction coefficients of X-shaped truss array channels of Scheme 3 show the same change trends with an increase in subchannel height ratio. Specifically, when the subchannel height ratio is less than 0.35, the friction coefficients of the channels gradually increase, and when the subchannel height ratio is greater than 0.35, the friction coefficients of the channels rapidly decreases. Therefore, when the subchannel height ratio is 0.35, the friction coefficients of X-shaped truss array channel of Scheme 3 at various Reynolds numbers are all the largest, indicating that the flow performance of the channel with a subchannel height ratio of 0.35 is the worst. When the subchannel height ratio is 0.20, the friction coefficients of the X-shaped truss array channel of Scheme 3 are the lowest, implying that the flow performance of the channel with a subchannel height ratio of 0.20 is the best. It can also be seen from Figure 7 that the friction coefficients of the X-shaped truss array channels of Scheme 3 slowly decrease with the increase in Reynolds number at different subchannel height ratios. Meanwhile, when the Reynolds numbers are 30,000 and 60,000, the friction coefficients of X-shaped truss array channels of Scheme 3 are very close to each other. In conclusion, when compared with the Reynolds number, the influence of subchannel height ratio on the flow performance of an X-shaped truss array channel is greater and more significant. From the perspective of reducing the friction coefficient, the X-shaped truss array channel with a small subchannel height ratio should be preferred.

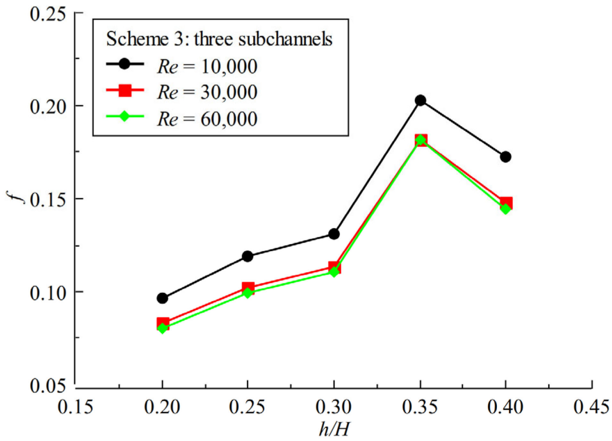

Figure 7. Effects of *h*/*H* on the flow performance of X-shaped truss array channels of Scheme 3 at different Reynolds numbers.

4.2. Heat Transfer Performance

Figure 8 illustrates the heat transfer distributions of X-shaped truss array channels of different layout schemes (see Table 1) at *Re* = 30,000. It can be seen from Figure 8 that the heat transfer distribution characteristics of the X-shaped truss array channels of three different layout schemes are similar. Specifically, due to the entrance effect (i.e., the heat transfer boundary layer at the channel inlet is very thin), the local Nusselt number of the channel wall is very high at the inlet, and then due to the gradual thickening of the heat transfer boundary layer, the local Nusselt number of the channel wall gradually decreases along the flow direction. Then, when the cooling air encounters the first row of truss units, the local Nusselt number of the channel wall rapidly increases due to the fluid-disturbing effect of the truss rods. The local Nusselt number of the channel wall at the location upstream of the truss rod ends is greatly improved. However, after the cooling air passes through the truss unit, the local Nusselt number of the corresponding channel wall in the downstream region of the truss unit is very low due to the blocking effect of the truss unit. Subsequently, the local Nusselt number on the channel wall shows a periodic, alternating distribution trend of high and low along the flow direction due to the array arrangement of truss units. For the whole channel wall, the local Nusselt number of the channel wall corresponding to the middle region of each row of truss units is lower, while the Nusselt number of the channel wall corresponding to both sides of each row of truss unis is higher. For truss units, the local Nusselt number on the windward side of each truss rod is high and the local Nusselt number on the leeward side of each truss rod is low. At the same time, along the flow direction, the local Nusselt number of each column of truss units slowly decreases. It can also be seen in Figure 8 that, from Scheme 1 to Scheme 3, the local Nusselt number of the truss unit slightly decreases or does not significantly change, while the local Nusselt number of the channel wall gradually increases. This may be caused by the gradual increase in the truss rod ends from Scheme 1 to Scheme 3, which has a great influence on the heat transfer effect of the channel wall.

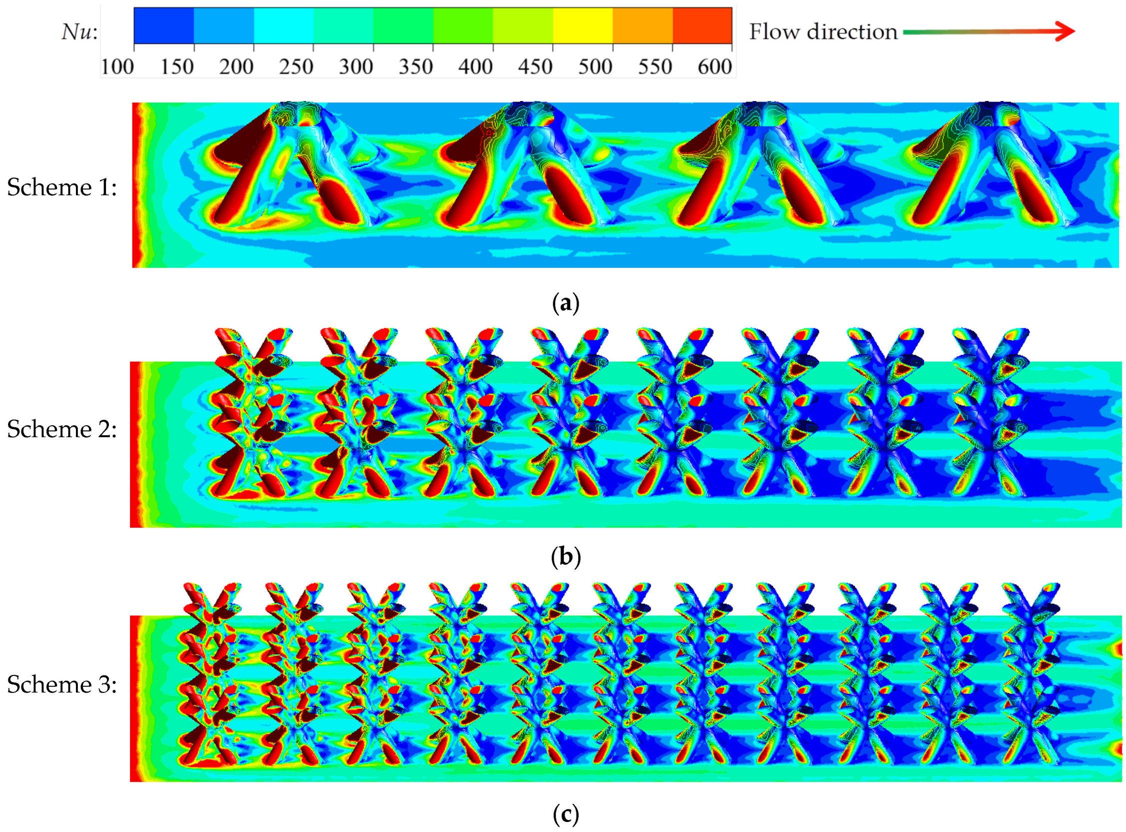

Figure 8. Heat transfer distributions of X-shaped truss array channels at different layout schemes (Re = 30,000): (**a**) Scheme 1; (**b**) Scheme 2; (**c**) Scheme 3.

Figure 9 shows the variation curves of average Nusselt numbers with inlet Reynolds number for the three layout schemes of X-shaped truss array channels, where Scheme 3 refers specifically to the channel of h/H = 0.35. As can be seen from Figure 9, with the increase in Reynolds number, the average Nusselt numbers of the three layout schemes of X-shaped truss array channels increase in a logarithmic form, that is, first increase rapidly and then slowly. This is because the increase in Reynolds number increases the flow velocity and disturbance effect of the cold fluid in the channel, which enhances the heat exchange between the cold fluid in the center of the channel and the hot fluid near the wall, and then strengthens the heat transfer performance of the channel. It can also be seen in Figure 9 that, among the three layout schemes of X-shaped truss array channels, the average Nusselt number of the channel of Scheme 3 is the highest and the corresponding heat transfer performance is the best, followed by the channels of Scheme 2 and Scheme 1. According to the quantitative calculation, when the Reynolds number increases from 10,000 to 60,000, the average Nusselt number of X-shaped truss array channels of Scheme 1, Scheme 2 and Scheme 3 increases by 2.45, 2.29 and 1.93 times, respectively. At different Reynolds numbers, when compared with the channels of Scheme 1 and Scheme 2, the average Nusselt numbers of the X-shaped truss array channels of Scheme 3 are increased from 38.94% to 63.49% and 5.68% to 18.65%, respectively. In conclusion, the layout scheme and Reynolds number both have a great influence on the heat transfer performance of the X-shaped truss array channel. From the perspective of heat transfer enhancement, the layout scheme of the X-shaped truss array channel of Scheme 3 is the best.

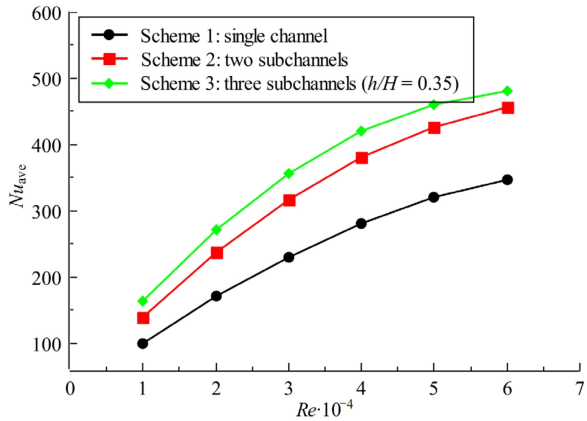

Figure 9. Comparison of the heat transfer performance of X-shaped truss array channels for different layout schemes.

Figure 10 displays the heat transfer distributions of X-shaped truss array channels of Scheme 3 at different subchannel height ratios (*Re* = 30,000). It can be seen from Figure 10 that, with the increase in subchannel height ratio, the number of truss units arranged in the channel gradually decreases. This leads to a gradual decrease in the number of regions with high heat transfer, as well as with low heat transfer on the channel wall, but the areas of these high-heat-transfer regions and low-heat-transfer regions gradually increase. For the channel wall, when the subchannel height ratio increases from 0.20 to 0.35, the local Nusselt number of the channel wall significantly increases. When the subchannel height ratio increases from 0.35 to 0.40, the local Nusselt number of the channel wall slightly decreases. For the truss unit, the variation trend of the local Nusselt number of the truss rod with the subchannel height ratio is basically the same as the variation trend of the local Nusselt number of the channel wall with the subchannel height ratio. The overall increase in the subchannel height ratio makes the difference in the local Nusselt number, which gradually decreases along the flow direction for both the channel wall and the truss units. Finally, the exact variation law of the heat transfer performance, along with the subchannel height ratio for the X-shaped truss array channels, needs to be determined by further quantitative analysis.

Figure 11 shows the variation curves of average Nusselt numbers with subchannel height ratio for the X-shaped truss array channel of Scheme 3 at different Reynolds numbers. As can be seen from Figure 11, under different Reynolds numbers, the average Nusselt number of X-shaped truss array channel of Scheme 3 first increases and then decreases with the increase in subchannel height ratio. When the subchannel height ratio is 0.35, the average Nusselt number of the channel of Scheme 3 is the highest. This implies that the heat transfer performance of the X-shaped truss array channel of Scheme 3 is the best at a subchannel height ratio of 0.35. When the subchannel height ratio is 0.20, the average Nusselt number of the channel of Scheme 3 is the lowest; that is, the heat transfer performance of the channel with a subchannel height ratio of 0.20 is the worst. According to the quantitative calculation, when the Reynolds number changes from 10,000 to 60,000, the average Nusselt numbers of the X-shaped truss array channel of Scheme 3 at a subchannel height ratio of 0.35 are from 26.79% to 37.70% and 9.56% to 11.34% higher than those at subchannel height ratios of 0.20 and 0.40, respectively. The above results are inconsistent with the influence laws of channel aspect ratio on the average Nusselt number of truss array channels reported in [36], previously published by the authors of the present study. The results in [36] show that the increase in channel aspect ratio reduces the average Nusselt number of truss array channels. The reason for the inconsistency of the above influence laws is that the aspect ratio of the entire cooling channel is constant, and the variation in subchannel height ratio changes the aspect ratio of the inner subchannels. This affects the distribution ratio of the cooling air from the entire cooling channel inlet between the truss array subchannels and the smooth subchannel. The distribution ratio of the cooling air may be the dominant factor affecting the heat transfer performance of the entire cooling channel because the design parameters of truss array structures in this study originate from the optimization results of the same modeled truss array channel with the same heat transfer performance as reported in the author's previously published paper [41]. Specifically, when $h/H \leq 0.35$, the cross-section areas of the truss array subchannels become larger with the increase in h/H, so that relatively more cooling air enters the truss array subchannels and improves the heat transfer performance of the entire cooling channel. When $h/H > 0.35$, although the increase in h/H also increases the cross-section areas of the truss array subchannels, the relevant increase in the size of the truss array structure may also bring more flow resistance, which reduces the cooling air entering the truss array subchannels and slightly weakens the heat transfer performance of the entire cooling channel.

It can also be seen from Figure 11 that, under different subchannel height ratios, the increase in Reynolds number significantly improves the average Nusselt number of X-shaped truss array channels of Scheme 3; that is, it effectively enhances the heat transfer performance of the X-shaped truss array channels. In conclusion, the subchannel height ratio has a relatively small effect on the heat transfer performance of X-shaped truss array channel of Scheme 3 when compared with the Reynolds number. From the perspective of heat transfer enhancement, the X-shaped truss array channel of Scheme 3 with a subchannel height ratio of 0.35 is the best.

4.3. Comprehensive Thermal Performance

Figure 12 shows the variation curves of comprehensive thermal coefficients with inlet Reynolds number for the three layout schemes of X-shaped truss array channels, where Scheme 3 refers specifically to the channel $h/H = 0.35$. As can be seen from Figure 12, the comprehensive thermal coefficients of X-shaped truss array channels rapidly decrease with the increase in Reynolds number. Among the three layout schemes of X-shaped truss array channels, the channel of Scheme 3 has the best comprehensive thermal performance, followed by the channel of Scheme 2, and the worst is the channel of Scheme 1. This is because among the three layout schemes, the channel of Scheme 3 has the highest average Nusselt number and a medium friction coefficient. Therefore, the channel of Scheme 3 has the highest comprehensive thermal coefficient. According to the quantitative analysis, when the Reynolds number varies from 10,000 to 60,000, the comprehensive thermal coefficients of X-shaped truss array channels of Scheme 1, Scheme 2 and Scheme 3 are reduced by 28.38%, 31.76% and 37.55%, respectively. Under different Reynolds numbers, the comprehensive thermal coefficients of the X-shaped truss array channel of Scheme 3 range from about 27.74% to 46.49% and 11.61% to 21.96% higher than those of the X-shaped truss array channels of Scheme 1 and Scheme 2, respectively. In summary, the layout scheme and Reynolds number both have significant effects on the comprehensive thermal performance of the X-shaped truss array channel; however, the influence degree of the layout scheme is slightly less than that of Reynolds number. The layout scheme of the X-shaped truss array channel of Scheme 3 is the most suitable choice when the reduction in friction coefficient and the enhancement of heat transfer are comprehensively considered.

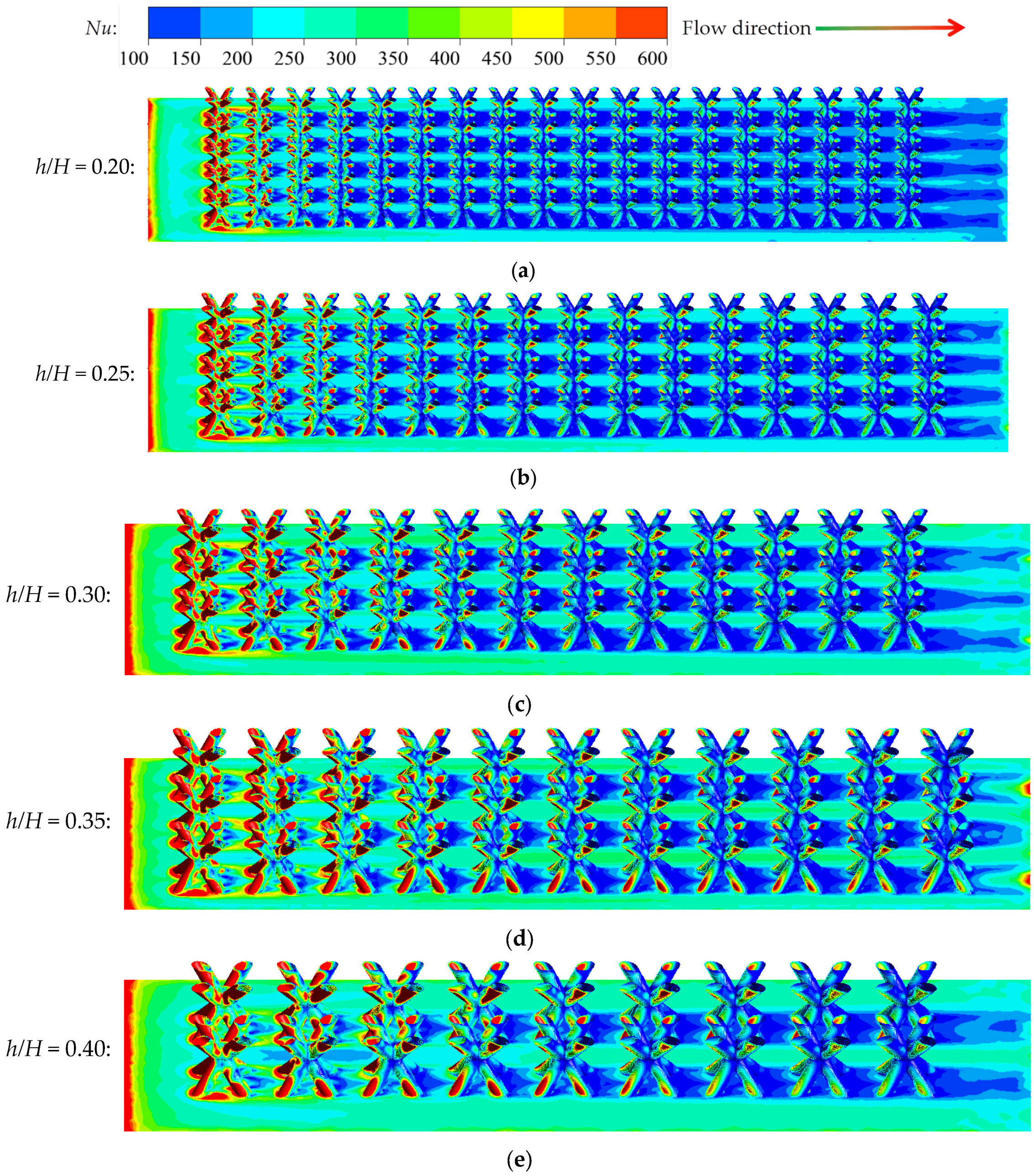

Figure 10. Heat transfer distributions of X-shaped truss array channels of Scheme 3 at different h/H (Re = 30,000): (**a**) h/H = 0.20; (**b**) h/H = 0.25; (**c**) h/H = 0.30; (**d**) h/H = 0.35; (**e**) h/H = 0.40.

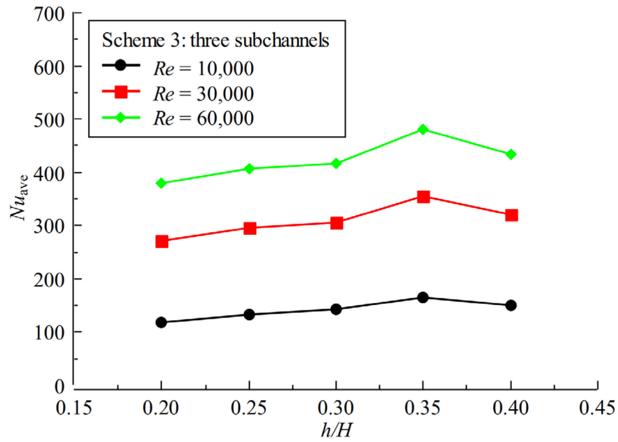

Figure 11. Effects of *h/H* on heat transfer performance of X-shaped truss array channels of Scheme 3 at different Reynolds numbers.

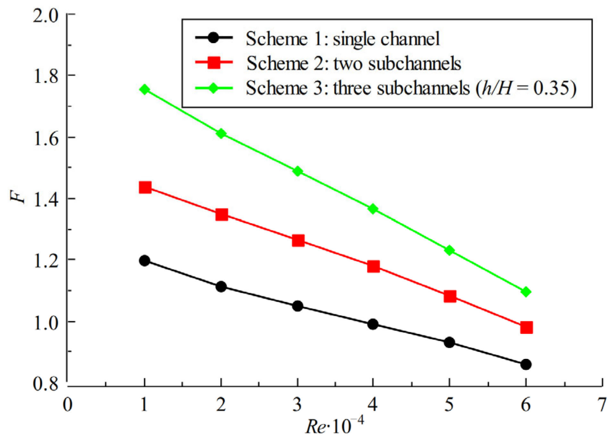

Figure 12. Comparison of comprehensive thermal performances of X-shaped truss array channels for different layout schemes.

Figure 13 displays the variation curves of a comprehensive thermal coefficient with a subchannel height ratio for the X-shaped truss array channel of Scheme 3 at different Reynolds numbers. It can be seen from Figure 13 that the increase in Reynolds number apparently weakens the comprehensive thermal performance of X-shaped truss array channel of Scheme 3. Under different Reynolds numbers, the influence laws of subchannel height ratio that affect the comprehensive thermal performance of the X-shaped truss array channel of Scheme 3 are not consistent. When the Reynolds number is low (Re = 10,000 and 30,000), the comprehensive thermal coefficient of the channel of Scheme 3 first slightly increases and then slightly decreases with the increase in subchannel height ratio. When the Reynolds number is high (Re = 60,000), the comprehensive thermal coefficient of the channel of Scheme 3 slowly decreases with the increase in subchannel height ratio. It is worth noting that, at a high Reynolds number, the comprehensive thermal performance of the X-shaped truss array channel of Scheme 3 with the subchannel height ratios of 0.20 and 0.25 is almost equal, and the heat transfer performance of the channel with a subchannel height ratio of 0.25 is better than that of the channel with a subchannel height ratio of 0.20 (see Figure 11). As a result of comprehensive consideration, the X-shaped truss array channel of Scheme 3 with a subchannel height ratio of 0.25 has a better overall cooling performance at a high Reynolds number and is more suitable for cooling the mid-chord region of gas turbine blades. In general, the effect of the Reynolds number on the comprehensive thermal performance of the X-shaped truss array channel of Scheme 3 is large, while the effect of subchannel height ratio on the comprehensive thermal performance of the channel of

Scheme 3 is not significant. The X-shaped truss array channel of Scheme 3 with a subchannel height ratio of 0.25 is most suitable to obtain the best overall cooling performance.

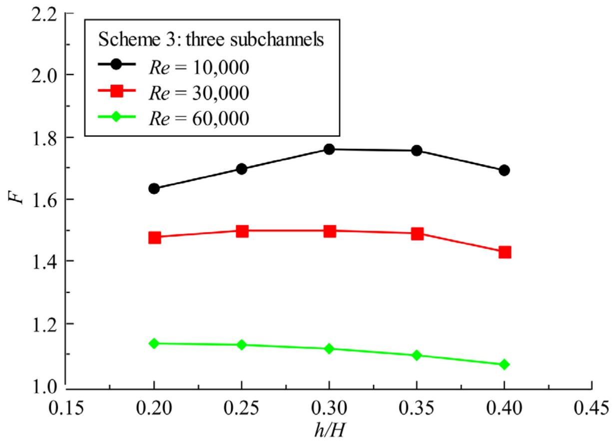

Figure 13. Effects of *h/H* on comprehensive thermal performance of X-shaped truss array channel of Scheme 3 at different Reynolds numbers.

4.4. Empirical Correlations

Fitting the heat transfer correlation and friction correlation of the X-shaped truss array cooling channel is of great significance to guide the design of the mid-chord cooling structure of heavy gas turbine blades in the future. As the parameters for each scheme of X-shaped truss array channels have little correlation, the empirical correlations reflecting the relationships between average Nusselt number, friction coefficient and Reynolds number should be separately fitted for each scheme of X-shaped truss array channel.

Based on the results from Sections 4.1–4.3, the power function was used to fit the correlations between the average Nusselt number, friction coefficient and Reynolds number for the three layout schemes of X-shaped truss array channels. The correlations between average Nusselt number, friction coefficient and Reynolds number can be assumed as:

$$f(x) = CRe^m \tag{9}$$

where $f(x)$ represents Nu_{ave} or f, and C and m are the parameters of the correlations to be fitted.

The fitting work is completed by the curve fit module of the Scipy package in Python 3.8. The parameters of Equation (9) obtained by fitting are listed in Table 3. R^2 is the determination coefficient; greater R^2 means higher goodness of fit. Table 3 shows that the fitting determination coefficients for the heat transfer correlations of each scheme of X-shaped truss array channels are all greater than 0.98, and those for the friction correlations are all higher than 0.86. Therefore, the parameters in Table 3 can provide a relatively accurate reference for the selection of a layout scheme for the X-shaped truss array channel.

Table 3. Fitting parameter values of heat transfer and friction correlation.

Channels	Nu_{ave}			f			***Re***
	C	***m***	R^2	***C***	***m***	R^2	
Scheme 1	0.163	0.700	0.995	0.172	−0.019	0.884	10,000 to 60,000
Scheme 2	0.286	0.675	0.991	0.258	−0.019	0.866	10,000 to 60,000
Scheme 3	0.605	0.614	0.985	0.351	−0.062	0.877	10,000 to 60,000

The relationships between the average Nusselt number, friction coefficient and Reynolds number for X-shaped truss array channels of Scheme 3 at different subchannel height ratios were also fitted based on Equation (9). The parameters of the fitted correlations are shown in Table 4. It can be seen from Table 4 that the determined coefficient of each correlation is greater than 0.87, which indicates that the heat transfer and friction correlations for X-shaped truss array channels of Scheme 3 at different subchannel height ratios all have a high goodness of fit.

Table 4. Fitting parameter values of heat transfer and friction correlation.

Channels	Nu_{ave}			f			Re
	C	m	R^2	C	m	R^2	
h/H = 0.20	0.229	0.659	0.987	0.240	−0.101	0.932	10,000 to 60,000
h/H = 0.25	0.396	0.637	0.986	0.294	−0.101	0.925	10,000 to 60,000
h/H = 0.30	0.532	0.612	0.987	0.305	−0.094	0.912	10,000 to 60,000
h/H = 0.35	0.605	0.614	0.985	0.351	−0.062	0.877	10,000 to 60,000
h/H = 0.40	0.589	0.606	0.987	0.418	−0.099	0.909	10,000 to 60,000

The heat transfer correlation and friction correlation corresponding to Table 4 can only reflect the influence law of the Reynolds number on the average Nusselt number and friction coefficient of X-shaped truss array channels of Scheme 3 with a special subchannel height ratio, but cannot reflect the influence law of subchannel height ratio. Therefore, the empirical correlations comprehensively reflect the influence laws of Reynolds number and subchannel height ratio on the average Nusselt number and friction coefficient of X-shaped truss array channels of Scheme 3, and were also fitted in this investigation. According to the results from Sections 4.1–4.3, the average Nusselt number and friction coefficient of the X-shaped truss array channels of Scheme 3 monotonically increase with the increase in Reynolds number, and first rapidly increase and then slightly decrease with the increase in subchannel height ratio. Therefore, the relationships of average Nusselt number and friction coefficient with Reynolds number and subchannel height ratio can be fitted by the power function, and the correlations of the average Nusselt number and friction coefficient with Reynolds number and subchannel height ratio can be assumed as follows:

$$f(x) = aRe^{b}(h/H)^{c} \tag{10}$$

where $f(x)$ represents Nu_{ave} and f, a, b, and c are the parameters to be fitted for the heat transfer and friction correlations.

Based on the numerical data in this study, the empirical correlations reflecting the effects of the Reynolds number and subchannel height ratio on the average Nusselt number and friction coefficient of the X-shaped truss array channel of Scheme 3 were also fitted by using the curve fit module of the Scipy package in Python (V3.8, Python Software Foundation, Wilmington, DE, USA). The fitting results are as follows:

$$Nu_{ave} = 1.1795Re^{0.5700}(h/H)^{0.2814} \tag{11}$$

$$f = 1.0532Re^{-0.08941}(h/H)^{0.9820} \tag{12}$$

The application scopes of the above fitted correlations are: $10{,}000 \leq Re \leq 60{,}000$, $0.20 \leq h/H \leq 0.40$.

Figure 14 shows the fitting error distribution of the Equations (11) and (12). It can be seen from Figure 14 that the fitting errors of heat transfer and friction correlations for the X-shaped truss array channels of Scheme 3 at different subchannel height ratios are within ±20%, in which the maximum error and mean error of the heat transfer correlation are 19.80% and 2.80%, the maximum error and mean error of the friction correlation are 13.20% and 5.30%, and the maximum error and mean error of the comprehensive thermal coefficients derived from the heat transfer and friction correlations are 19.70% and 2.04%, respectively. Therefore, the empirical correlations fitted in this study can accurately predict the average Nusselt number, friction coefficient and comprehensive thermal coefficient of the X-shaped truss array cooling channels of Scheme 3. The above results can provide a reference for the design of X-shaped truss array channels in the mid-chord region of gas turbine blades.

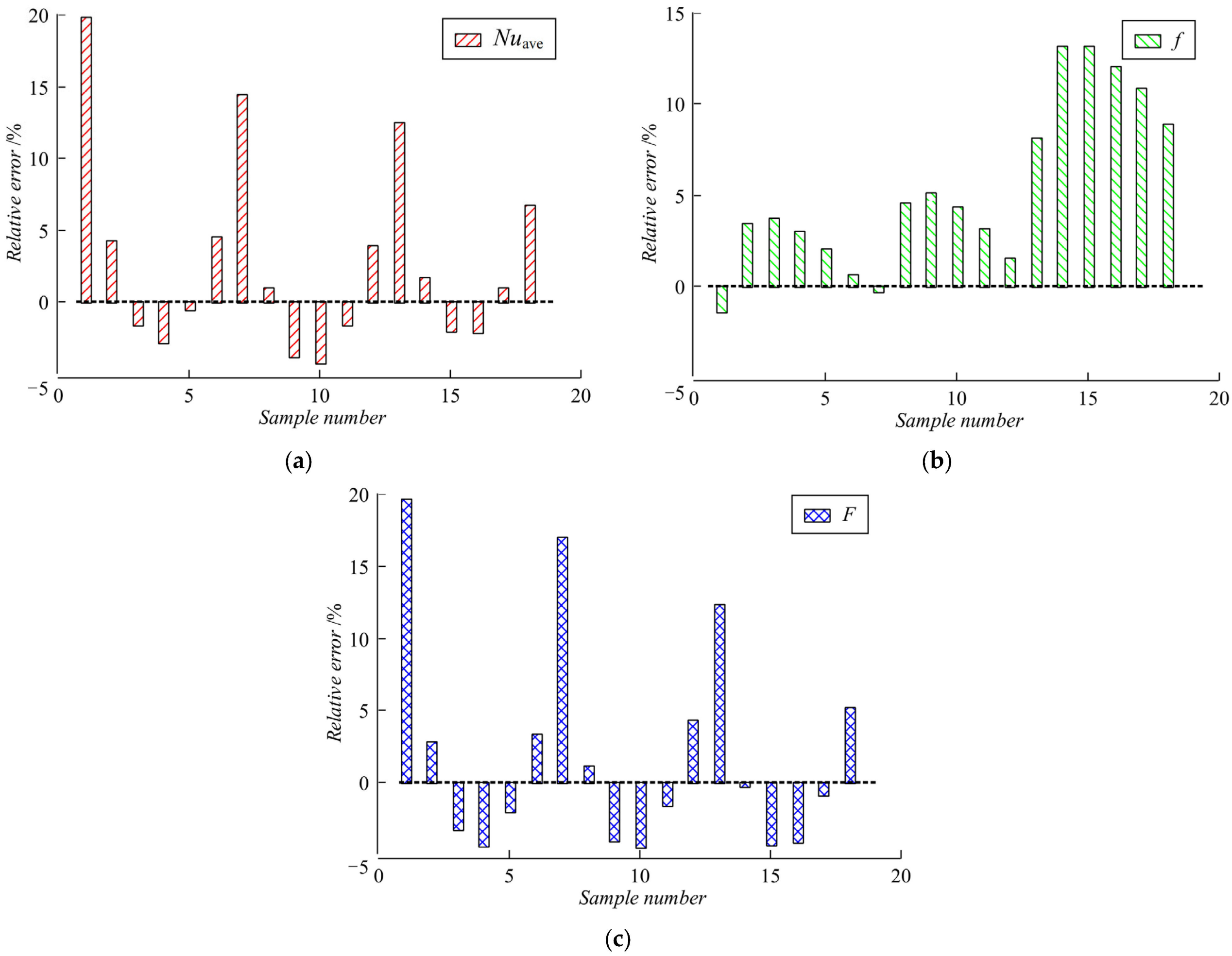

Figure 14. Fitting errors: (**a**) C_p; (**b**) *Nu*; (**c**) *F*.

5. Conclusions

In this work, the flow and heat transfer performance of cooling channels filled with X-shaped truss array structures were numerically investigated at different layout schemes. The main findings from the results are as follows:

(1) Among the three layout schemes of X-shaped truss array channels, the channel of Scheme 1 has the best flow performance, while the channel of Scheme 3 has the best heat transfer performance and comprehensive thermal performance.

(2) At different Reynolds numbers, the average Nusselt numbers and comprehensive thermal coefficients of the X-shaped truss array channel of Scheme 3 range from 38.94% to 63.49% and 27.74% to 46.49% higher than those of Scheme 1, and from 5.68% to 18.65% and 11.61% to 21.96% higher than those of Scheme 2.

(3) With the increase in subchannel height ratio, the friction coefficient and average Nusselt number of the X-shaped truss array channel of Scheme 3 both show a trend of first increasing and then decreasing, while the comprehensive thermal coefficient shows a slow decreasing trend at higher Reynolds numbers.

(4) As a result of comprehensive consideration, the X-shaped truss array channel of Scheme 3 at h/H = 0.25 has a better overall cooling performance and is more suitable for cooling the mid-chord region of gas turbine blades.

(5) The layout scheme has significant effects on the flow performance, heat transfer performance and comprehensive thermal performance of X-shaped truss array channels. The subchannel height ratio has a great influence on the flow performance, but has a relatively small influence on the heat transfer performance and comprehensive thermal performance of the channel.
(6) The heat transfer and friction correlations of X-shaped truss array cooling channels were obtained under different layout schemes, which may provide a reference for the application of truss array structures in the internal cooling of advanced high-temperature turbine blades in the future.

Author Contributions: Conceptualization, L.X. (Lei Xi) and J.G.; methodology, L.X. (Lei Xi); validation, L.X. (Lei Xi), J.G. and L.X. (Liang Xu); formal analysis, Z.Y.; investigation, Z.Z.; resources, J.G.; data curation, Z.Z.; writing—original draft preparation, L.X. (Lei Xi); writing—review and editing, Z.Z.; visualization, Z.Y.; supervision, Y.L. and L.X. (Lei Xi); project administration, Y.L. and J.G. All authors have read and agreed to the published version of the manuscript.

Funding: The authors would like to express their sincere gratitude to the Project Supported by Natural Science Basic Research Plan in Shaanxi Province of China (2022JQ-545), the Project funded by China Postdoctoral Science Foundation (2021M702573) and the National Natural Science Foundation of China (51876157) for providing financial support for this work.

Institutional Review Board Statement: Not applicable.

Informed Consent Statement: Not applicable.

Data Availability Statement: Not applicable.

Conflicts of Interest: The authors declare no conflict of interest.

Nomenclature

C	truss unit characteristic length, mm
d	truss rod diameter, mm
f	friction coefficient
f_0	friction coefficient of the smooth channel
F	comprehensive thermal coefficient
h	subchannel height, mm
H	channel height, mm
L	channel length, mm
Nu	local Nusselt number
Nu_{ave}	average Nusselt number
Nu_0	average Nusselt number of the smooth channel
p_{in}	channel inlet pressure, Pa
p_{out}	channel outlet pressure, Pa
q	heat flux, $\mathrm{W \cdot m^{-2}}$
Re	inlet Reynolds number
T_{f}	reference temperature, K
T_{w}	wall temperature, K
u	inlet velocity, $\mathrm{m \cdot s^{-1}}$
W	channel width, mm
X_{s}	transverse spacing, mm
Z_{s}	streamwise spacing, mm
Greek symbols	
β	inclination angle of truss rod, °
δ	thickness of channel wall, mm
Δp	pressure difference between channel inlet and outlet, Pa
λ	air thermal conductivity, $\mathrm{W \cdot m^{-1} \cdot K^{-1}}$
ρ	air density, $\mathrm{kg \cdot m^{-3}}$
v	air kinematic viscosity, $\mathrm{m^2 \cdot s^{-1}}$

References

1. Wu, W.; Yao, R.; Wang, J.; Su, H.; Wu, X. Leading edge impingement cooling analysis with separators of a real gas turbine blade. *Appl. Therm. Eng.* **2022**, *208*, 118275. [CrossRef]
2. Han, J.C. Advanced cooling in gas turbines 2016 Max Jakob memorial award paper. *J. Heat Trans. T ASME* **2018**, *140*, 113001. [CrossRef]
3. Nourin, F.N.; Amano, R.S. Review of gas turbine internal cooling improvement technology. *J. Energ. Resour.-ASME* **2021**, *143*, 080801. [CrossRef]
4. Zhang, J.; Zhang, S.; Wang, C.; Tan, X. Recent advances in film cooling enhancement: A review. *Chin. J. Aeronaut.* **2020**, *33*, 1119–1136. [CrossRef]
5. Ye, L.; Liu, C.L.; Jiang, P.X.; Zhu, Y.H. Heat transfer characteristics in a trailing-edge slot cooling surface with outward protrusions. *Exp. Heat Transf.* **2022**, *35*, 1–20. [CrossRef]
6. Li, Y.; Liu, T.; Tao, J.; Yang, W.; Dong, L. Heat transfer characteristics in a narrow confined channel with discrete impingement cooling. *Chin. J. Aeronaut.* **2022**, *35*, 220–229. [CrossRef]
7. Zhang, G.; Zhu, R.; Xie, G.; Li, S.; Sunde, B. Optimization of cooling structures in gas turbines: A review. *Chin. J. Aeronaut.* **2022**, *35*, 18–46. [CrossRef]
8. Zhang, W.; Zhu, H.; Li, G. Experimental study of heat transfer on the internal surfaces of a double-wall structure with pin fin array. *Energies* **2020**, *13*, 6573. [CrossRef]
9. Xi, L.; Gao, J.; Xu, L.; Zhao, Z.; Ruan, Q.; Li, Y. Numerical investigation and parameter sensitivity analysis on flow and heat transfer performance of jet array impingement cooling in a quasi-leading-edge channel. *Aerospace* **2022**, *9*, 87. [CrossRef]
10. Gasparetto, V.E.; ElSayed, M.S. Multiscale optimization of specific elastic properties and microscopic frequency band-gaps of architectured microtruss lattice materials. *Int. J. Mech. Sci.* **2021**, *197*, 106320. [CrossRef]
11. Di Caprio, F.; Acanfora, V.; Franchitti, S.; Sellitto, A.; Riccio, A. Hybrid Metal/Composite Lattice Structures: Design for Additive Manufacturing. *Aerospace* **2019**, *6*, 71. [CrossRef]
12. Di Caprio, F.; Franchitti, S.; Borrelli, R.; Bellini, C.; Di Cocco, V.; Sorrentino, L. Ti-6Al-4V Octet-Truss Lattice Structures under Bending Load Conditions: Numerical and Experimental Results. *Metals* **2022**, *12*, 410. [CrossRef]
13. Li, J.; Huang, Z.; Liu, G.; An, Q.; Chen, M. Topology optimization design and research of lightweight biomimetic three-dimensional lattice structures based on laser powder bed fusion. *J. Manuf. Process.* **2022**, *74*, 220–232. [CrossRef]
14. Daynes, S.; Feih, S. Bio-inspired lattice structure optimisation with strain trajectory aligned trusses. *Mater. Design* **2022**, *213*, 110320. [CrossRef]
15. Guo, J.; Li, Y.; Xiao, Y.; Fan, Y.; Yu, D.; Wen, J. Multiscale modeling and design of lattice truss core sandwich metastructures for broadband low-frequency vibration reduction. *Compos. Struct.* **2022**, *289*, 115463. [CrossRef]
16. Wang, S.; Ma, Y.; Deng, Z.; Wu, X. Two elastically equivalent compound truss lattice materials with controllable anisotropic mechanical properties. *Int. J. Mech. Sci.* **2022**, *213*, 106879. [CrossRef]
17. Shangguan, H.; Kang, J.; Yi, J.; Zhang, X.; Wang, X.; Wang, H.; Huang, T. The Design of 3D-Printed Lattice-Reinforced Thickness-Varying Shell Molds for Castings. *Materials* **2018**, *11*, 535. [CrossRef]
18. Shahrzadi, M.; Emami, M.D.; Akbarzadeh, A.H. Heat transfer in BCC lattice materials: Conduction, convection, and radiation. *Compos. Struct.* **2022**, *284*, 115159. [CrossRef]
19. Le, V.T.; Ha, N.S.; Goo, N.S. Advanced sandwich structures for thermal protection systems in hypersonic vehicles: A review. *Compos. Part B Eng.* **2021**, *226*, 109301. [CrossRef]
20. Luo, S.; Xu, D.; Song, J.; Liu, J. A review of regenerative cooling technologies for scramjets. *Appl. Therm. Eng.* **2021**, *190*, 116754. [CrossRef]
21. Kim, T.; Hodson, H.P.; Lu, T.J. Contribution of vortex structures and flow separation to local and overall pressure and heat transfer characteristics in an ultralightweight lattice material. *Int. J. Heat Mass Transf.* **2005**, *48*, 4242–4264. [CrossRef]
22. Wei, K.; He, R.; Cheng, X.; Pei, Y.; Zhang, R.; Fang, D. Fabrication and heat transfer characteristics of C/SiC pyramidal core lattice sandwich panel. *Appl. Therm. Eng.* **2015**, *81*, 10–17. [CrossRef]
23. Gao, L.; Sun, Y.G. Thermal control of composite sandwich structure with lattice truss cores. *J. Thermophys. Heat Tr.* **2015**, *29*, 47–54. [CrossRef]
24. Gao, L.; Sun, Y.; Cong, L. Active cooling performance of all-composite lattice truss core sandwich structure. *Heat Transf. Res.* **2016**, *47*, 1093–1108. [CrossRef]
25. Dixit, T.; Nithiarasu, P.; Kumar, S. Numerical evaluation of additively manufactured lattice architectures for heat sink applications. *Int. J. Therm. Sci.* **2020**, *159*, 106607. [CrossRef]
26. Qian, B.; Fan, H.; Liu, G.; Zhang, J.; Li, P. Microchannel Liquid-Cooled Heat Exchanger Based on a Nonuniform Lattice: Study on Structure Calculation, Formation Process, and Boiling Heat Transfer Performance. *Materials* **2021**, *14*, 7248. [CrossRef]
27. Son, Y.W.; Kim, T.; Lu, T.J.; Chang, S.M. On thermally managing lithium-ion battery cells by air-convection aspirated in tetrahedral lattice porous cold plates. *Appl. Therm. Eng.* **2021**, *189*, 116711. [CrossRef]
28. You, J.H.; Park, K. Design and additive manufacturing of thermal metamaterial with high thermal resistance and cooling capability. *Addit. Manuf.* **2021**, *41*, 101947. [CrossRef]
29. Yun, S.; Lee, D.; Jang, D.S.; Lee, M.; Kim, Y. Numerical analysis on thermo-fluid–structural performance of graded lattice channels produced by metal additive manufacturing. *Appl. Therm. Eng.* **2021**, *193*, 117024. [CrossRef]

30. Kaur, I.; Singh, P. Critical evaluation of additively manufactured metal lattices for viability in advanced heat exchangers. *Int. J. Heat Mass Transf.* **2021**, *168*, 120858. [CrossRef]
31. Kaur, I.; Singh, P. Endwall heat transfer characteristics of octahedron family lattice-frame materials. *Int. Commun. Heat Mass* **2021**, *127*, 105522. [CrossRef]
32. Zhou, M.; Geng, D. Multi-scale and multi-material topology optimization of channel-cooling cellular structures for thermomechanical behaviors. *Comput. Methods Appl. Mech. Eng.* **2021**, *383*, 113896. [CrossRef]
33. Lai, X.; Wang, C.; Peng, D.; Yang, H.; Wei, Z. Analysis of heat transfer characteristics of a heat exchanger based on a lattice filling. *Coatings* **2021**, *11*, 1089. [CrossRef]
34. Xu, L.; Chen, H.; Xi, L.; Xiong, Y.; Gao, J.; Li, Y. Flow and heat transfer characteristics of a staggered array of Kagome lattice structures in rectangular channels. *Heat Mass Transf.* **2022**, *58*, 41–64. [CrossRef]
35. Hussain, S.; Ghopa, W.A.W.; Singh, S.S.K.; Azman, A.H.; Abdullah, S. Experimental and Numerical Vibration Analysis of Octet-Truss-Lattice-Based Gas Turbine Blades. *Metals* **2022**, *12*, 340. [CrossRef]
36. Xu, L.; Ruan, Q.; Shen, Q.; Xi, L.; Gao, J.; Li, Y. Optimization design of lattice structures in internal cooling channel with variable aspect ratio of gas turbine blade. *Energies* **2021**, *14*, 3954. [CrossRef]
37. Xu, L.; Shen, Q.; Ruan, Q.; Xi, L.; Gao, J.; Li, Y. Optimization design of lattice structures in internal cooling channel of turbine blade. *Appl. Sci.* **2021**, *11*, 5838. [CrossRef]
38. Kaur, I.; Aider, Y.; Nithyanandam, K.; Singh, P. Thermal-hydraulic performance of additively manufactured lattices for gas turbine blade trailing edge cooling. *Appl. Therm. Eng.* **2022**, *211*, 118461. [CrossRef]
39. Liang, D.; He, G.; Chen, W.; Chen, Y.; Chyu, M.K. Fluid flow and heat transfer performance for micro-lattice structures fabricated by Selective Laser Melting. *Int. J. Therm. Sci.* **2022**, *172*, 107312. [CrossRef]
40. Xi, L.; Xu, L.; Gao, J.; Zhao, Z.; Li, Y. Study on flow and heat transfer performance of X-type truss array cooling channel. *Case Stud. Therm. Eng.* **2021**, *26*, 101034. [CrossRef]
41. Xi, L.; Xu, L.; Gao, J.; Zhao, Z.; Li, Y. Cooling performance analysis and structural parameter optimization of X-shaped truss array channel based on neural networks and genetic algorithm. *Int. J. Heat Mass Transf.* **2022**, *186*, 122452. [CrossRef]
42. Xu, L.; Wang, W.; Gao, T.; Gao, J. An experimental research on the cooling performance of the turbine vane with an advanced duplex-medium combined cooling. *Int. J. Heat Mass Transf.* **2014**, *79*, 72–81. [CrossRef]
43. Gao, T.; Zeng, J.; Li, J.; Gong, J. Numerical prediction on mist/steam cooling in a square ribbed channel at real gas turbine operational conditions. *Int. J. Heat Mass Transf.* **2017**, *108*, 1089–1102. [CrossRef]